Electronic Engineering of Amorphous Fe-Co-S Sites in Hetero-nanoframes for Oxygen Evolution and Flexible Al-air Batteries

Min Lu, Li An, Jie Yin, Jing Jin, Rui Yang, Bolong Huang, Yang Hu, Yong-Qin Zhao, Pinxian Xi,* and Chun-Hua Yan*

M. Lu, L. An, J. Yin, J. Jin, R. Yang, Y. Hu, Prof. Y.-Q. Zhao, Prof. P. Xi, Prof. C.-H. Yan
State Key Laboratory of Applied Organic Chemistry,
Frontiers Science Center for Rare Isotopes,
College of Chemistry and Chemical Engineering,
Lanzhou University,
Lanzhou 730000, China
E-mail: xipx@lzu.edu.cn

Prof. B. Huang
Department of Applied Biology and Chemical Technology,
The Hong Kong Polytechnic University,
Hung Hum, Kowloon, Hong Kong SAR, China
E-mail: bhuang@polyu.edu.hk

Prof. C.-H. Yan
Beijing National Laboratory for Molecular Sciences,
State Key Laboratory of Rare Earth Materials Chemistry and Applications,
PKU-HKU Joint Laboratory in Rare Earth Materials and Bioinorganic Chemistry,
College of Chemistry and Molecular Engineering,
Peking University,
Beijing 100871, China

Keywords: ((amorphous, hetero-nanoframes, oxygen evolution, Al-air batteries))

Aluminum-air batteries have been considered to be a promising power candidate for flexible electronics. And the performance of Al-air batteries is mainly regulated by the catalytic activity of air electrode catalysts. Here, we demonstrate electronic engineered amorphous Fe-Co-S sites embedded in Prussian blue analogues ($FeCoS_x$-PBA) hetero-nanoframes. The experimental results and DFT calculations reveal the critical role of the introduced $FeCoS_x$ layer to PBA, which enhances the electron transfer and alleviates the overbinding effect of OH* during the oxygen evolution reaction (OER). The $FeCoS_x$-PBA hybrid system supplies an optimized electronic structure for the alkaline OER, which is also confirmed by the much-lowered overpotential (266 mV at 10 mA cm^{-2}) for the alkaline OER. Furthermore, the flexible Al-air battery based on $FeCoS_x$-PBA cathode catalyst exhibits a high peak power density (58.3 mW cm^{-2}), energy density (1483 Wh kg_{Al}^{-1}), and outstanding stability for more than 50 h operation

under bending or stretching condition, demonstrating its potential in the practical application of flexible electronic devices. Our results may provide a new strategy of modulating the electronic structure of air electrode catalysts to efficiently promote the reactivity of alkaline OER and Al-air batteries process.

1. Introduction

The rapid development of flexible and wearable electronic equipment promotes the exploitation of highly efficient energy storage and conversion devices such as aluminum (Al)-air batteries. It has remarkable advantages of high theoretical energy density, excellent safety, and low cost compared to traditional batteries (such as lithium-ion batteries and zinc-air batteries). The oxygen involved reaction is the most crucial process for Al-air batteries in portable devices and electric vehicles.[1-4] However, the related oxygen involved electro-process is usually restricted by the instinctly sluggish kinetics for multiple-step proton-coupled electron transfer steps.[5-10] Therefore, developing highly efficient catalysts with excellent activity and predominant durability is critical for its practical applications. Although noble metal and metal oxides (Pt, Ir, and IrO_2) exhibit state-of-the-art catalytic activities for the oxygen involved process, their multiple disadvantages, including high cost, scarcity, and poor durability, limit their application on a commercial scale.[11] For this purpose, the development of low-cost and highly active transition metal-based catalysts is essential.[12-16]

Hetero-nanoframes consisted of hollow frame structures have been considered as an essential morphology in nanocatalysts due to their abundant exposed active sites, enhanced mass/charge transfer velocity, reduced possibility of aggregation, and favorable interface effects.[17-19] However, the poor intrinsic catalytic performance is still a challenge for their application in electrocatalysis. Cation and anion exchange is an efficient approach to modify the inherent electronic structure and create new active sites through the introduction of hetero-atoms, thus improve the intrinsic catalytic activity. After the introduction of heteroatoms, the

surface electron density of active sites can be changed due to the variational coordination environment among neighboring atoms accompanied by the mismatch of electronegativity and ionic radius.[20] Accordingly, a tailored electronic configuration with optimized band structure and abundant defects can be adjusted into catalysts through precisely ion-exchange strategy, which is favorable to promote catalytic activity.[21-23]

In our work, an amorphous $FeCoS_x$ embedded in Prussian blue analogues hetero-nanoframes ($FeCoS_x$-PBA) was fabricated through an ultrasound-assisted ion-exchange method. By engineering electronic structure through hetero-ion introduction (Fe^{2+} and S^{2-}) and amorphization, the $FeCoS_x$-PBA catalyst has enchanced electron transfer capability and optimized binding strength with intermediates. Besides, it's unique hetero-nanoframes morphology also provide more exposed active sites. As-obtained material exhibits excellent oxygen evolution performance with a low overpotential of 266 mV at 10 mA cm^{-2} and superior durability. Dynamic OER study unravel the important role of S atoms to OER of the $FeCoS_x$-PBA catalyst. Through DFT calculations, the obvious change of the electronic structures was unraveled, which indicates the boosted electronic conductivity to promote the electron/charge transfer during OER. Meanwhile, the surface unsaturated $FeCoS_x$ layer demonstrates the optimized binding strength of OH, leading to the alleviated energy barrier of the rate-determining step for OER. In addition, when severed as air cathode catalyst in Al-air batteries, the $FeCoS_x$-PBA shows the promoted battery performance. A remarkably high discharge power density of 58.3 mW cm^{-2}, a large energy density of 1483 Wh kg^{-1} and excellent long-term stability for more than 50 h operation after mechanical recharge was achieved. More importantly, all-solid-state Al-air batteries with excellent bendability and stretchability are assembled and applied to charge a smartphone successfully.

2. Result and Discussion

$FeCoS_x$-PBA hetero-nanoframes were synthesized by a sequential ultrasound-assisted ion-exchange method. The initial PBA nanocubes ultrasonic in dilute HCl solution containing Fe^{2+}, leading to the partial replacement of Co^{2+} with Fe^{2+} in PBA surface and formed Fe/Co mixed Prussian blue analogues (MPBA) nanocubes, which provides a basis for the further synthesis of $FeCoS_x$ structure. Further solvothermal treatment was performed to achieve S^{2-} ion exchange with $Fe(CN)_6^{3-}$.

The crystal structure of PBA, MPBA, and $FeCoS_x$-PBA (**Figure 1a**) was studied by X-ray diffraction (XRD). The results of all three samples show the same diffraction pattern as $K_2CoFe(CN)_6$ (JCPDS#75-38) and $Fe_4[Fe(CN)_6]_3$ (JCPDS#73-687), which can be indexed to a cubic structure with *F-43m* symmetry. Due to an almost coincident lattice structure between $K_2CoFe(CN)_6$ and $Fe_4[Fe(CN)_6]_3$, MPBA shows no noticeable change in XRD pattern compared to PBA. Furthermore, after the introduction of S, $FeCoS_x$-PBA also shows the same XRD pattern with PBA and MPBA, demonstrating that the major components of $FeCoS_x$-PBA are still $K_2CoFe(CN)_6$ and $Fe_4[Fe(CN)_6]_3$. During the solvothermal reaction process, low concentration S^{2-} was released from thioacetamide (TAA). Then S^{2-} inactivated by ethanol, favors the incomplete decomposition of MPBA, resulting the retain of partial the Prussian blue structure.[24-27] It is worth noting that all XRD peaks shift mildly from MPBA to $FeCoS_x$-PBA, as shown in **Figure 1a**. The main diffraction peak at 2θ = 17.57° of MPBA shifts to 17.43° of $FeCoS_x$-PBA, revealing the expansion of lattice distance caused by the successful introduction of hetero cation (Fe^{2+}) and anion (S^{2-}).

The morphology was study by scanning electron microscopy (SEM) and transmission electron microscopy (TEM). The results show PBA exhibits nanocubes morphology with a diameter of about 250 nm (**Figure S1**). After Fe^{2+} ion exchange, MPBA nanocubes with a nearly unchanged diameter and morphology (**Figure S2**). The Fe^{2+} ion exchange process was also studied by the same ultrasonic experiment without the addition of Fe^{2+}. As seen, The PBA nanocubes were corroded and broken into porous nanocubes (**Figure S3**). The above results

indicated that Fe^{2+} has a stronger bonding than Co^{2+} with $[Fe(CN)_6]^{3-}$ and it can resist the corrosion of HCl, which drives the Fe^{2+} ion exchange process. After ion exchange with S^{2-}, The SEM image of $FeCoS_x$-PBA in **Figure 1b** clearly shows a typical cubic shape with numerous small nanoparticles attached on the surface. TEM image further confirms the hollow cube-like structure of $FeCoS_x$-PBA with an outer diameter of about 250 nm and skeleton thickness of 20-40 nm. The attached surface nanoparticles were ranging from 30 nm to 50 nm. Brunner−Emmet−Teller (BET) results (**Figure S4 and Table S1**) also support hollow structure of $FeCoS_x$-PBA, which has a significantly increased BET surface area.

To determine the structural changes caused by the introduction of S. The TEM was further performed on $FeCoS_x$-PBA. The remarkable single crystal structure with the cubic system was also confirmed by the selected area electron diffraction (SAED) images in the *inset* of **Figure 1c**. Combined with XRD results, it indicated that the hollow cube is mainly an MPBA structure. The energy-dispersive X-ray spectroscopy (EDX) element scan demonstrates the uniform distribution of Fe, Co, and S of $FeCoS_x$-PBA (**Figure 1d**). The line scan profile of a single $FeCoS_x$-PBA hetero-nanoframes indicated the distribution of Fe, Co, and S. The S content is significantly high in surface nanoparticles and much lower in the skeleton part. It suggests the surface nanoparticles may be $FeCoS_x$. High-Resolution Transmission Electron Microscopy (HRTEM) was used to study the lattice structure of $FeCoS_x$-PBA further. As shown in **Figure 1e**, no lattice fringe can be observed of the surface particle. Its corresponding Fast Fourier Transform (FFT) image (insert of **Figure 1e**) also shows no diffraction spots, revealing the amorphous feature of $FeCoS_x$. The amorphous structure also evidenced by contrast experiment, MPBA react with Na_2S instead of TAA in the same experiment condition to fully convert prussian blue to sulfide. As-obtained materials show no XRD peak (**Figure S5**), revealing the amorphous structure.

The skeleton part of $FeCoS_x$-PBA displayed legible lattice fringes, which can be ascribed to (200) plane of $K_2CoFe(CN)_6$ and $Fe_4[Fe(CN)_6]_3$ in **Figure 1f and S6**. Three parts marked as

green, blue, and red frame were chosen to remove background noise by Inverse Fourier Filtering method and was shown in **Figure 1g, h, and i**. **Figure 1g** shows significant lattice distortions marked byline and a large area of vacancies defects marked by dots. **Figure 1h** displays characteristic lattice dislocations of ~0.23 nm, which the periodic arrangement of atoms mismatches and slides. **Figure 1i** illustrates a representative HRTEM image, in which the marked lattice spacing value is 0.516 nm that assigned to (200) plane of prussian blue structure. Compared to PBA and MPBA with lattice distance of 0.504 nm and 0.506 nm respectively, $FeCoS_x$-PBA shows a small lattice expansion of 0.01 nm, it may attribute to the flexible and framework-like lattice structure of ferricyanide. These S^{2-} doping and the resulting abundant lattice imperfection were proved to exist in $FeCoS_x$-PBA and could be expected to promote the electrocatalytic performance.[28-30] Element mapping in **Figure 1j-m** also demonstrate the distribution of Fe, Co, S in $FeCoS_x$-PBA.

The above results indicated that the S atom has two primary forms in $FeCoS_x$-PBA. One is S^{2-} in $FeCoS_x$, another is doped S in Prussian blue. X-ray photoelectron spectroscopy (XPS) was performed to provide in-depth evidence and trace the electronic structure difference among PBA, MPBA, and $FeCoS_x$-PBA (**Figure 2a-e, S7**). Along with S introduction, the Co 2p spectra of $FeCoS_x$-PBA in **Figure 2a** were deconvoluted into two pairs of the peak at the binding energies of 778.3 eV, 781.1 eV, 793.3 eV, and 797.3 eV, which were attributed to Co-S and Co-N species, respectively.[31-32] Fe 2p spectra of $FeCoS_x$-PBA (**Figure 2b**) show a similar structure with Co. The peaks at 708.1 eV and 720.7 eV belonged to Fe-C species, while the peaks at 708.5 eV and 721.8 eV belonged to Fe-S species.[33-35] Moreover, S 2p spectra of $FeCoS_x$-PBA (**Figure 2c**) can be identified as two pairs of the peak with binding energies of 161.8 eV, 163.0 eV, 163.9 eV, and 165.0 eV. The former two peaks can be assigned to Fe/Co-S groups, and the latter two belong to C-S groups.[29] From these results, it can be found that doped S atom in $FeCoS_x$-PBA bond with the C atom of the cyanide ligands to form C-S structure. This suggestion was further confirmed by C 1s XPS spectra, a new peak center at 285.6 eV is

observed for $FeCoS_x$-PBA and can be assigned to the C-S structure (**Figure S8**).[36] Other peaks at 284.6 eV, 286.7 eV, and 288.7 eV are attributed to C=C-C, C-O/C-N, and C=O, respectively.[37-38] Besides, the N coordination was verified by the N 1s spectra. Three types of nitrogen peaks of $FeCoS_x$-PBA were fitted at 397.1 eV, 398.3 eV, and 401.8 eV, which are attributed to Fe/Co-N, C-N, and N-H species.[39-40] Furthermore, a significant peak shift was observed after S introduction. Original Co-N and Fe-C peaks appear to be a negative shift of 0.8 eV and 0.5 eV, indicating the increased electron density of Co and Fe atoms. The electrical effect of S atoms was further spread to the adjacent N and C atoms. The negative shift and positive peak shift of N and C, respectively, revealed the electron density in C and N atoms decreased and increased separately. Besides, a significant enhanced N-H peak at 401.8 eV was observed in $FeCoS_x$-PBA also demonstrates N atoms become more electronegative and more accessible to combine hydrogen molecules in the atmosphere to form N-H like species.[40] above results further support the two primary forms of S in $FeCoS_x$-PBA.

To further detail the local electronic structure, EELS was performed. Especially for the $FeCoS_x$-PBA, the PBA frame region and amorphous $FeCoS_x$ particles region was studied separately (**Figure S9)**. First, the Fe $L_{2,3}$ white lines (**Figure 2e**) shows 0.5 eV negitively shift from MPBA to PBA, which indicate a slightly decreased of valence state of Fe. This is consistent with the introduction of Fe^{2+} in MPBA. Thus, the Co and Fe $L_{2,3}$ spectra of PBA frame region in $FeCoS_x$-PBA has no sigficant change compared with MPBA, it shows the doped S don't influence the valence state of Co and Fe. But the Co and Fe $L_{2,3}$ spectra of amorphous $FeCoS_x$ region in $FeCoS_x$-PBA exhit 1 eV positive shift compared with PBA frame region. Represents a significant structural difference between PBA structure and sulfide structure.[41] The S $L_{2,3}$ white lines (**Figure 2f**) intensity in PBA frame region is lower than amorphous $FeCoS_x$ region and has 0.5 eV difference. Which also shows the different forms of S in $FeCoS_x$-PBA. [42-44] The Mössbauer spectroscopy was further employed to analyze different Fe species. The Mössbauer spectrum of $FeCoS_x$-PBA (**Figure 2f**) was fitted with a single and a doublet

assigned to Fe (II)-C/N and Fe (II)-S species, respectively. The Mössbauer spectrum of PBA and MPBA (**Figure S10, S11**) were fitted with a single and a doublet but assigned to low spin Fe (II) and high spin Fe (III) species, respectively.[35,45-46] After introducing Fe^{2+}, the region ratio of single: doublet in MPBA increased, showing an increased Fe^{2+}/Fe^{3+} ratio from 1.46 to 2.91. The corresponding fitting parameters and the relative peak area for the catalysts were summarized in **Table S2**.

Then we introduce the DFT calculations to unravel the significant improvements of OER performance in the $FeCoS_x$-PBA hybrid system. Although the cage structure of PBA endows them a stable structure with a high surface area, the low electronic conductivity still leads to limited application in the electrocatalyst. With the introduction of the $FeCoS_x$ on the surface with different bonding situations, the electroactivity of PBA has been activated on the surface defective $FeCoS_x$ layer with large exposure of active sites. The bonding and anti-bonding orbitals near the Fermi level (E_F) are mostly dominated by the surface $FeCoS_x$ layers. Meanwhile, the remarkable stability of the PBA structure frame determines the long-term durability of the composite electrocatalyst (**Figure 3a**). Thus, the projected partial density of states (PDOS) of S, Fe, Co, and -CN functional groups in $FeCoS_x$-PBA are illustrated. Except for the surface, S sites demonstrate the broad S-3p orbitals, covering from E_V-8.0 eV to E_V+3.5 eV (E_V=0 eV). However, the surface unsaturated S shows a strong delocalization feature with the dominant peak at E_V-4.7 eV, which effectively suppresses the overbinding effect of -OH in the alkaline environment (**Figure 3b**). From the bulk to the surface, the e_g of Fe-3d orbitals significantly shifting from E_V+4.5 eV to E_V+0.6 eV. The downshifting of the d-band center of surface Fe is also noted, which boosts up both the electron transfer and binding with the OH group. Meanwhile, the surface Fe indicates the evident crossing of E_F, supporting the reduction of valence state with improved electronic conductivity. This significantly compensates for the poor electron transfer capability in pristine PBA (**Figure 3c**). For Co-3d orbitals, we notice the evident splitting of t_2g and e_g in PBA-Co and the interfacial Co. Only Co sites in the surface

$FeCoS_x$ layer demonstrate the increased electron density of 3d orbitals near E_F to further enhance the electron transfer, which is consistent with the XPS results (**Figure 3d**). In addition, the CN groups in PBA is also investigated regarding the electronic structures. From the bulk PBA to the interfacial region binding with $FeCoS_x$, the s,p orbitals of -CN groups demonstrate the gradual downshift away from the E_F, becoming more electronegative, which confirms the experimental characterizations. This also means that the introduction of the surface $FeCoS_x$ layers not only leads to the modified -CN functional groups with improved stability but also the overbinding poisoning of OH groups during OER (**Figure 3e**).

The OER activity was studied in an alkaline medium (1.0 M KOH) through linear sweep voltammetry (LSV) (**Figure 4a**) for the as-prepared three catalysts and benchmark Ir/C (20%) which were prepared on glassy carbon electrodes. After modifying PBA's outermost surface by Fe^{2+}, the as-obtained MPBA has an obvious enhanced catalytic performance with 75 mV increased overpotential at 10 mA cm^{-2} compared with PBA. Furthermore, the $FeCoS_x$-PBA with further optimization of electronic structure and decreased *d*-band center shows the best OER activity among all these samples, including commercial Ir/C. Its overpotential at a current density of 10 mA cm^{-2} is approximately 266 mV, much lower than Ir/C (320 mV), PBA (409 mV), and MPBA (334 mV), respectively. The Tafel plot is an inherent parameter to evaluate OER catalytic kinetics. The lowest Tafel slope of 33 mV dec^{-1} (**Figure 4b**) for $FeCoS_x$-PBA suggested the fastest OER dynamics. Long-term stability is another crucial criterion factor in evaluating the catalytic property. Hence, the chronoamperometric response was carried out at a constant current density of ~8 mA cm^{-2}. After 15 hours test, $FeCoS_x$-PBA still remains 91.4% current, indicate its superior durability (**Figure S12**). To eliminate the influence of corrosion current, a faradaic efficiency study was performed on a rotating ring-disk electrode (RRDE) in N_2-saturated 1 M KOH (**Figure S13**). With the disk current held constant at 200 μA, a ring current of ~38.3 μA was detected, which proved that the observed OER current catalyzed by $FeCoS_x$-PBA could be mainly attributed to OER with high Faradaic efficiency of 95.7%.

To gain deeper insight into the OER activity of the $FeCoS_x$-PBA, the electrochemical impedance spectra (EIS) and electrochemical double-layer capacitance (C_{dl}) test was performed. The C_{dl} of $FeCoS_x$-PBA, MPBA, and PBA (**Figure S14**) is confirmed to be 24.3 mF cm^{-2}, 11.8 mF cm^{-2}, and 8.2 mF cm^{-2}, respectively. Combine with BET results (**Figure S4**), the $FeCoS_x$-PBA performed better exposure and enhanced electroactive sites. In the Nyquist plots (**Figure 4c**), PBA displays the largest charge transfer resistance (R_{ct}), and MPBA shows a 12% reduced R_{ct} value. Undoubtedly, $FeCoS_x$-PBA owns the lowest R_{ct} of all three catalysts. It is only approximately a quarter of PBA, which suggested that the faster electron transfer ability during OER in $FeCoS_x$-PBA. This result further proved that the electron structure was modified from PBA to $FeCoS_x$-PBA along with decreasing R_{ct}. The important role of PBA frameworks to OER also unravel by contrast experiment. As shown in **Figure S15**, amorphous $FeCoS_x$ shows poor OER activities compared to $FeCoS_x$-PBA.

The OER dynamic study is another vital tool to understand the OER process and mechanism. *In-situ* Raman and *quasi-in-situ* XPS spectrum was performed on $FeCoS_x$-PBA during the OER catalysis process. *In-situ* Raman spectrum (**Figure 4d and S16**) shows a catalysts' reconstruction in 1.35 V (vs. RHE) and formed CoFe oxy-hydroxides. The low reconstruction voltage is in favor of catalyzing OER and could be caused by large amount defects in amorphous structure. Further *quasi-in-situ* XPS results unravel the electronic structure evolution of different elements at different applied OER voltage. As shown in **Figure 4e**, with the increased voltage, the valence state of Co also grows and becomes stable at a high value. But Fe offers a very steady valence state among the OER process. These results show the Co sites facilitate the site-to-site electron transfer and stabilize the Fe sites. Moreover, the S 2p *quasi-in-situ* XPS result (**Figure 4e and S17)** shows the existence of residual sulfur in catalysts during OER. Which means the surface reconstituted species is S doped CoFe oxy-hydroxides or CoFe hydroxysulfides. The increased adsorbed SO_4^{2-} peak also indicated lattice

S in $FeCoS_x$-PBA is partially oxidized into SO_4^{2-} during OER. The SO_4^{2-} would be adsorbed on the catalyst surface and promote the OER process.[47-50]

Then we further unravel the improved electroactivity of the $FeCoS_x$-PBA hybrid system based on the energetic reaction pathway. Under the equilibrium state, the OER reaction pathway shows the continuous trend for both PBA and $FeCoS_x$-PBA composite systems. The reaction [*O+H_2O+2OH] → [*OOH+H_2O+OH] is the rate-determining step for OER due to the largest energy barrier. For pure PBA, the energy barrier is 1.78 eV which is much larger than the 1.47 eV of $FeCoS_x$-PBA composite system, confirming the enhanced electroactivity for OER (**Figure 4g**). With the applied standard potential of 1.23 V, the evident reaction trend is displayed. For pristine PBA, the initial OH adsorption of alkaline OER is very strong, which leads to a nearly 1 eV energy drop. However, such a strong overbinding effect of OH also hinders the subsequent reactions, resulting in 0.55 eV overpotential of the OER. In comparison, although the slightly weaker adsorption of OH on $FeCoS_x$-PBA composite shows the initial uphill trend for OER, the overall overpotential has been much lowered to 0.24 eV, which is highly consistent with the electrochemical performances (**Figure 4h**). The stable adsorption of key intermediates shows that the O-related species prefer the Fe sites on the surface with mild adsorption strength to maintain efficient intermediates transformation. Meanwhile, the Co sites facilitate the site-to-site electron transfer from the surface, and S sites balance the optimal binding strength with OH groups within the alkaline environment. Which is consistent with the *quasi-in-situ* XPS results (**Figure 4e, f and S17**). The stable structure of PBA after adsorption supports the long-term durability performances in the experiments (**Figure 4i**).

To evaluate the Al-air battery performance of $FeCoS_x$-PBA. A liquid Al-air battery was assembled in which 2 M KOH with ZnO and Na_2SnO_3 as additive was used as the electrolyte to slow down the corrosion of aluminum,[51] an aluminum sheet and $FeCoS_x$-PBA/carbon black loaded on carbon cloth (2 mg cm^{-2}) served as the anode and air cathode, respectively. Polarization curves (**Figure 5b**) indicated that the maximum power density of $FeCoS_x$-PBA is

58.3 mW cm^{-2}. The capacity property was studied by Galvanostatic discharge curves. As shown in **Figure 5c**, $FeCoS_x$-PBA generates a large specific capacity of 1259 mAh g^{-1} at a current density 1 mA cm^{-2}, and the energy density was calculated as 1483 Wh kg^{-1}. When current density increased to 5 mA cm^{-2}, the specific capacity and energy density also decreased to 1091 mAh g^{-1} and 1199 Wh kg^{-1}, respectively. Furthermore, in a large discharge current density of 10 mA cm^{-2}, this Al-air battery still remains 1002 mAh g^{-1} capacity and 970 Wh kg^{-1}energy density. These battery parameters of $FeCoS_x$-PBA materials are better than other materials in the literature to the best of our knowledge and indicated their great potential to serve as efficient air cathodes for clean energy storage and conversion applications. Due to the extremely high reduction potential of Al in aqueous, Al cannot be electrodeposited in aqueous electrolytes. Thus, the Al-air battery was not rechargeable. Hence, to assess the long-term stability of $FeCoS_x$-PBA cathode, a mechanical recharge through replacing Al sheet was performed. 10 hours was chosen as a period, and in all 5 periods, the Al-air battery remains nearly unchanged in discharge voltage, as shown in **Figure 5d**. This result demonstrated that $FeCoS_x$-PBA cathode exhibit superior long-term stability. Further, the blue light-emitting diode was successfully lighted by two-series-connected Al-air batteries (**Figure S18**). Also, the Ragone diagram plotting the energy and power densities of the fabricated device compared to those reported Al-air batteries is depicted in **Figure 5e** and **Table S4**.

Driven by the increasing demand for flexible and wearable electronic devices, solid Al-air batteries were further fabricated with $FeCoS_x$-PBA/carbon black material supported on carbon cloth as the air cathode, aluminum sheet as the metal anode, and alkaline polyvinyl alcohol/polyethylene glycol as the gel electrolyte. The fabricated battery exhibits outstanding bendability and stretchability. **Figure 5f** shows a single battery displays an open circuit voltage of 1.44 V, and two batteries in series exhibit an open-circuit voltage of 2.94 V. The hydrogel used in batteries endows the battery with excellent flexibility (**Figure S19**). At a discharge current of 1 mA, this solid Al-battery was bent to 60, 120, and 180 degrees respectively and its

discharge performance is almost constant because its discharge voltage only has slightly decreased (**Figure 5g**). When the battery was stretched by 10%, 20%, and 30%, it did not break upon elongation. After stretched 10% to 30%, the battery has a gradually decreased discharge voltage at 1 mA cm^{-2}, but the voltage decreasing amplitude is small. Even up to 30%, the battery output voltage was also maintained above 1 V during stretching (**Figure 5h**). It is easy to understand that stretch batteries will increase charge and mass transfer distance and hinder battery performance. From the above results, this solid flexible Al-air battery displays remarkable bendability and stretchability. The actual application shows that the device with four batteries connected in series can charge a smartphone from 20% electricity to fully charge (**Figure 5i**) under various bending conditions from 0^o to 360^o.

3. Conclusion

In summary, we have successfully developed a unique hollow $FeCoS_x$-PBA hetero-nanoframes catalyst via an ultrasound-assisted ion exchange procedure. Through the introduction of Fe and S atoms, abundant defects were created. Besides, the original atoms with the modified electronic structure caused the obvious downward shift d-band center, which decrease the adsorption and desorption energy between active sites and catalytic intermediates. DFT calculations further confirm that the surface $FeCoS_x$ layer significantly enhances the electron transfer capability of PBA to achieve the efficient OER process. The suppression of OH overbinding also guarantees the transformation of the efficient intermediate. Meanwhile, the stable structure of PBA protected by the surface $FeCoS_x$ layer is the critical factor for the long-term durability of electrocatalysts. Above morphological and structural advantages provide more exposed active sites and optimize the intrinsic electronic structure, which dramatically enhances the catalytic activity. Moreover, $FeCoS_x$-PBA cathode can drive a solid Al-air battery with remarkable bendability, stretchability, and a high specific capacity of 1259 mAh g^{-1} at 1 mA cm^{-2}. This work may expand the toolbox of the strategy to design and synthesize high-

performance energy-related catalysts in morphology and structure through electronic engineering.

Supporting Information
Supporting Information is available from the Wiley Online Library or from the author.

Acknowledgements
We acknowledge support from the National Natural Science Foundation of China (No. 21931001 and 21922105), the Special Fund Project of Guiding Scientific and Technological Innovation Development of Gansu Province (2019ZX-04) and the 111 Project (B20027). We also acknowledge support by the Fundamental Research Funds for the Central Universities (lzujbky-2021-pd04, lzujbky-2021-it12 and lzujbky-2021-37). B.H. acknowledges the support of the Natural Science Foundation of China (NSFC) (No. 21771156) and the Early Career Scheme (ECS) fund (Grant PolyU 253026/16P) from the Research Grant Council (RGC) in Hong Kong. J.Y. acknowledges the support of the China Postdoctoral Science Foundation (2021M691375) and the China National Postdoctoral Program for Innovative Talents (BX20200157).

Received: ((will be filled in by the editorial staff))
Revised: ((will be filled in by the editorial staff))
Published online: ((will be filled in by the editorial staff))

References

[1] C. Steven, A. Majumdar, *Nature*. **2012**, *488*, 294.

[2] J. Suntivich, H. A. Gasteiger, N. Yabuuchi, H. Nakanishi, J. B. Goodenough, S. H. Yang, *Nat. Chem.* **2011**, *3*, 546.

[3] A. Kudo, Y. Miseki, *Chem. Soc. Rev.* **2009**, *38*, 253.

[4] F. Meng, H. Zhong, D. Bao, J. Yan, X. Zhang, *J. Am. Chem. Soc.* **2016**, *138*, 10226.

[5] M. W. Kanan, D. G. Nocera, *Science.* **2008**, *321*, 1072.

[6] J. Jin, J. Yin, H. Liu, P. Xi, *Chinese J. Catal.* **2019**, *40,* 43.

[7] J. Yin, B. Wei, Y. Li, Y. Li, P. Xi, *J. Energy Chem.* **2019**, *34*, 1.

[8] J. Yin, J. Jin, H. Liu, B. Huang, M. Lu, J. Li, H. Liu, H. Zhang, Y. Peng, P. Xi, C.-H. Yan, *Adv. Mater.* **2020**, *32*, 2001651.

[9] L. An, B. Huang, Y. Zhang, R. Wang, N. Zhang, T. Dai, P. Xi, C.-H. Yan, *Angew. Chem. Int. Ed.* **2019**, *58*, 9459.

[10] L. An, Z. Zhang, J. Feng, F. Lv, Y. Li, R. Wang, M. Lu, R. B. Gupta, P. Xi, S. Zhang, *J. Am. Chem. Soc.* **2018**, *140*, 17624.

[11] Y. Lee, J. Suntivich, K. J. May, E. E. Perry, S. H. Yang, *J. Phys. Chem.* **2012**, *3*, 399.

[12] J. Suntivich, K. J. May, H. A. Gasteiger, J. B. Goodenough, S. H. Yang, *Science.* **2011**, *334*, 1383.

[13] F. Cheng, J. Chen, *Chem. Soc. Rev.* **2012**, *41*, 2172.

[14] T.Y. Ma, S. Dai, M. Jaroniec, S. Z. Qiao, *J. Am. Chem. Soc.* **2014**, *136*, 13925.

[15] J. Xie, J. Zhang, S. Li, F. Grote, X. Zhang, H. Zhang, R. Wang, Y Lei, B. Pan, Y. Xie, *J. Am. Chem. Soc.* **2013**, *135*, 17881.

[16] R. Yang, L. An, Y. Zhang, N. Zhang, T. Dai, P. Xi, *ChemCatChem* **2019**, *11*, 6002.

[17] X. Y. Yu, Y. Feng, Y. Jeon, B. Guan, X. W. D. Lou, U. Paik, *Adv. Mater.* **2016**, *28*, 9006.

[18] J. Nai, Y. Lu, L. Yu, X. Wang, X. W. D. Lou, *Adv. Mater.* **2017**, *29*, 1703870.

[19] D. S. He, D. He, J. Wang, Y. Lin, P. Yin, X. Hong, Y. Wu, Y. Li, *J. Am. Chem. Soc.* **2016**, *138*, 1494.

[20] S. Liu, M. Wang, X. Sun, N. Xu, J. Liu, Y. Wang, T. Qian, C. Yan, *Adv. Mater.* **2018**, *30*, 12876.

[21] V. R. Stamenkovic, B. Fowler, B. Simon Mun, G. Wang, P. N. Ross, C. A. Lucas, N. M. Marković, *Science.* **2007**, *315*, 493.

[22] B. Hammer, J. K. Nørskov, Surface *Science.* **1995**, *343*, 211.

[23] F. Cheng, J. Shen, B. Peng, Y. Pan, Z. Tao, J. Chen, *Nat. Chem.* **2011**, *3*, 79.

[24] L. Han, X. Y. Yu, X. W. Lou, *Adv. Mater.* **2016**, *28*, 4601.

[25] X. Y. Yu, L. Yu, H. B. Wu, X. W. Lou, *Adv. Mater.* **2015**, *127*, 5421.

[26] G. Yilmaz, K. M. Yam, C. Zhang, H. J. Fan, G. W. Ho, *Adv. Mater.* **2017**, *29*, 1606814.

[27] X. Xu, F. Song, X. Hu, *Nat. Commun.* **2016**, *7*, 12324.

[28] Y. Ito, W. Cong, T. Fujita, Z. Tang, M. Chen, *Angew. Chem. Int. Ed.* **2015**, *54*, 2131.

[29] Y. Dou, T. Liao, Z. Ma, D. Tian, Q. Liu, F. Xiao, Z. Sun, J. Ho Kim, S. Xue Dou, *Nano Energy.* **2016**, *30*, 267.

[30] Y. Liu, H. Cheng, M. Lyu, S. Fan, Q. Liu, W. Zhang, Y. Zhi, C. Wang, C. Xiao, S. Wei, B. Ye, Y. Xie, *J. Am. Chem. Soc.* **2014**, *136*, 15670

[31] Z. Chen, Y. Song, J. Cai, X. Zheng, D. Han, Y. Wu, Y. Zang, S. Niu, Y. Liu, J. Zhu, X. Liu, G. Wang, *Angew. Chem. Int. Ed.* **2018**, *57*, 5076.

[32] F. Cao, M. Zhao, Y. Yu, B. Chen, Y. Huang, J. Yang, X. Cao, Q. Lu, X. Zhang, Z. Zhang, C. Tan, H. Zhang, *J. Am. Chem. Soc.* **2016**, *138*, 6924.

[33] Y. Chen, R. Gokhale, A. Serov, K. Artyushkova, P. Atanassov, *Nano Energy.* **2017**, *38*, 201.

[34] Y. Li, Y. Wang, B. Pattengale, J. Yin, L. An, F. Cheng, Y. Li, J. Huang, P. Xi, *Nanoscale.* **2017**, *9*, 9230.

[35] H. Shen, E. Gracia-Espino, J. Ma, K. Zang, J. Luo, L. Wang, S. Gao, X. Mamat, G. Hu, T. Wagberg, S. Guo, *Angew. Chem. Int. Ed.* **2017**, *56*, 13988.

[36] D. R. Mullins, P. F. Lyman, *J. Phys. Chem.* **1993**, *97*, 9226.

[37] J. Yin, Q. Fan, Y. Li, F. Cheng, P. Zhou, P. Xi, S. Sun, *J. Am. Chem. Soc.* **2016**, *138*, 14546.

[38] H. Zhang, S. Hwang, M. Wang, Z. Feng, S. Karakalos, L. Luo, Z. Qiao, X. Xie, C. Wang, D. Su, Y. Shao, G. Wu, *J. Am. Chem. Soc.* **2017**, *139*, 14143.

[39] J. Yin, Y. Li, F. Lv, Q. Fan, Y. Q. Zhao, Q. Zhang, W. Wang, F. Cheng, P. Xi, S. Guo, *ACS Nano.* **2017**, *11*, 2275.

[40] L. Wang, W. Zhang, X. Zheng, Y. Chen, W. Wu, J. Qiu, X. Zhao, X. Zhao, Y. Dai, J. Zeng, *Nat. Energy.* **2017**, *2*, 869.

[41] T.-H. Shen, L. Spillane, J. Vavra, T. H. M. Pham, J. Peng, Y. Shao-Horn, V. Tileli, *J. Am. Chem. Soc.* **2020**, *142*, 15876.

[42] W. Sohn, K. C. Kwon, J. M. Suh, T. H. Lee, K. C. Roh, H. W. Jang, *Nano Converg.* **2021**, *8*, 11.

[43] K. Urita, T. Fujimori, H. Notohara, I. Moriguchi, *ACS Appl. Energy Mater.* **2018**, *1*, 807.

[44] Z. Yang, Z. Zhu, J. Ma, D. Xiao, X. Kui, Y. Yao, R. Yu, X. Wei, L. Gu, Y.-S. Hu, H. Li, X. Zhang, *Adv. Energy Mater.* **2016**; *6*, 1600806.

[45] W. Wang, J. Jiang, T. Ding, C. Wang, J. Zuo, Q. Yang, *ACS Appl. Mater. Inter.* **2015**, *7*, 2235.

[46] U. I. Kramm, M. Lefevre, N. Larouche, D. Schmeisser, J. P. Dodelet, *J. Am. Chem. Soc.* **2014**, *136*, 978.

[47] M. W. Louie, A. T. Bell, *J. Am. Chem. Soc.* **2013**, *135*, 12329.

[48] B. S. Yeo, A. T. Bell, *J. Am. Chem. Soc.* **2011**, *133*, 5587.

[49] A. Moysiadou, S. Lee, C.-S. Hsu, H. M. Chen, X. Hu, *J. Am. Chem. Soc.* **2020**, *142*, 11901.

[50] N. Kornienko, J. Resasco, N. Becknell, C.-M. Jiang, Y.-S. Liu, K. Nie, X. Sun, J. Guo, S. R. Leone, P. Yang, *J. Am. Chem. Soc.* **2015**, *137*, 7448.

[51] Y. Xu, Y. Zhao, J. Ren, Y. Zhang, H. Peng, *Angew. Chem. Int. Ed.* **2016**, *128*, 8111.

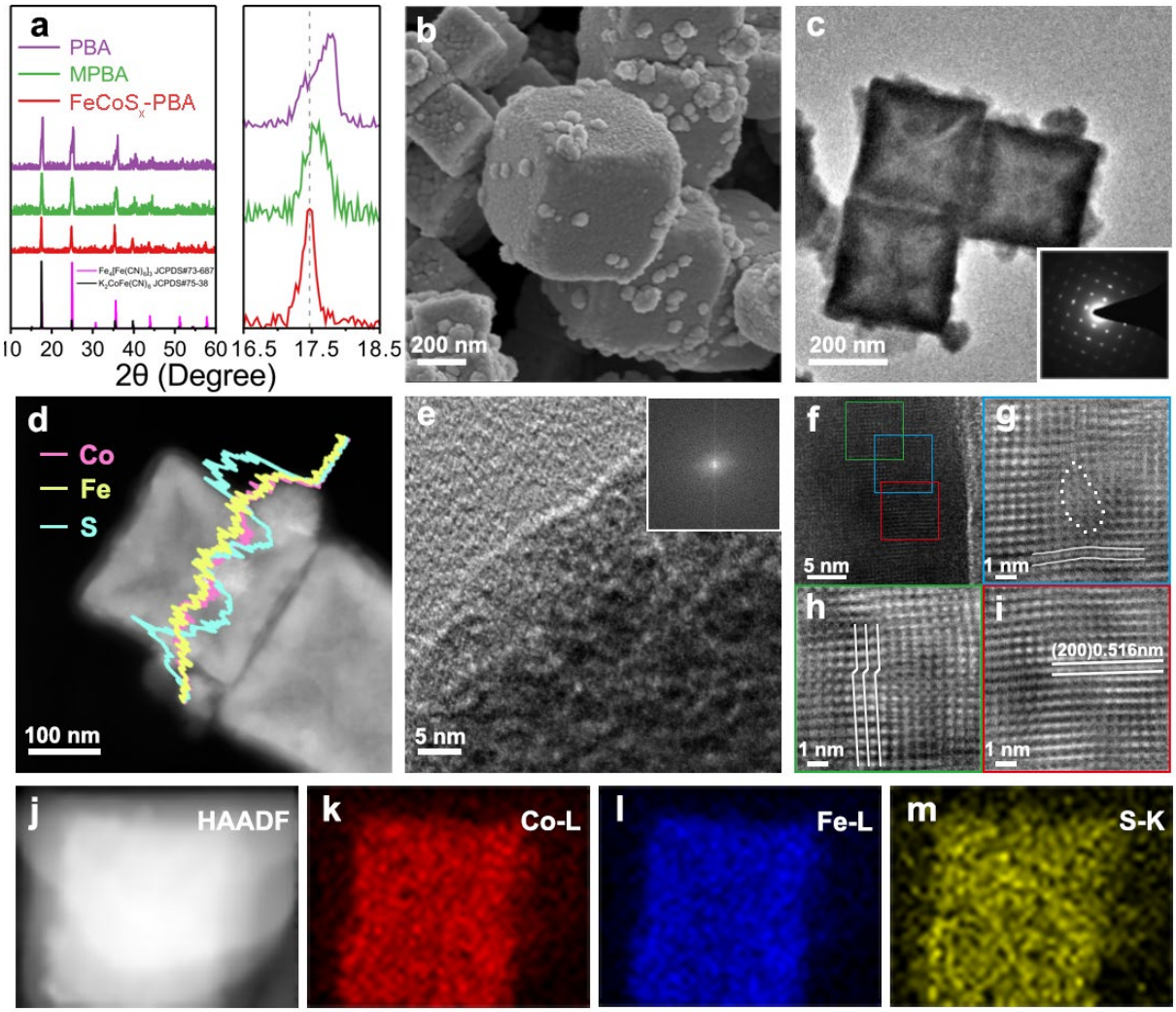

Figure 1. (a) Powder XRD pattern of PBA, MPBA, and $FeCoS_x$-PBA (left). The corresponding XRD pattern range from 16 degrees to 19 degrees (right). (b) SEM image of $FeCoS_x$-PBA. (c) TEM image of $FeCoS_x$-PBA, and the corresponding SAED image (inset). (d) EDX line scan of a single $FeCoS_x$-PBA hetero-nanoframes. (e) HRTEM image of nanoparticle in the surface of $FeCoS_x$-PBA, and the corresponding FFT image (inset). (f) HRTEM image of the skeleton part in $FeCoS_x$-PBA. (g-i) magnified HRTEM images extracted by Inverse Fourier Filtering of blue, red and green box in (f). EDX mapping of $FeCoS_x$-PBA in (j) HAADF-image, (k) Co L edge, (i) Fe L edge, (m) S K edge.

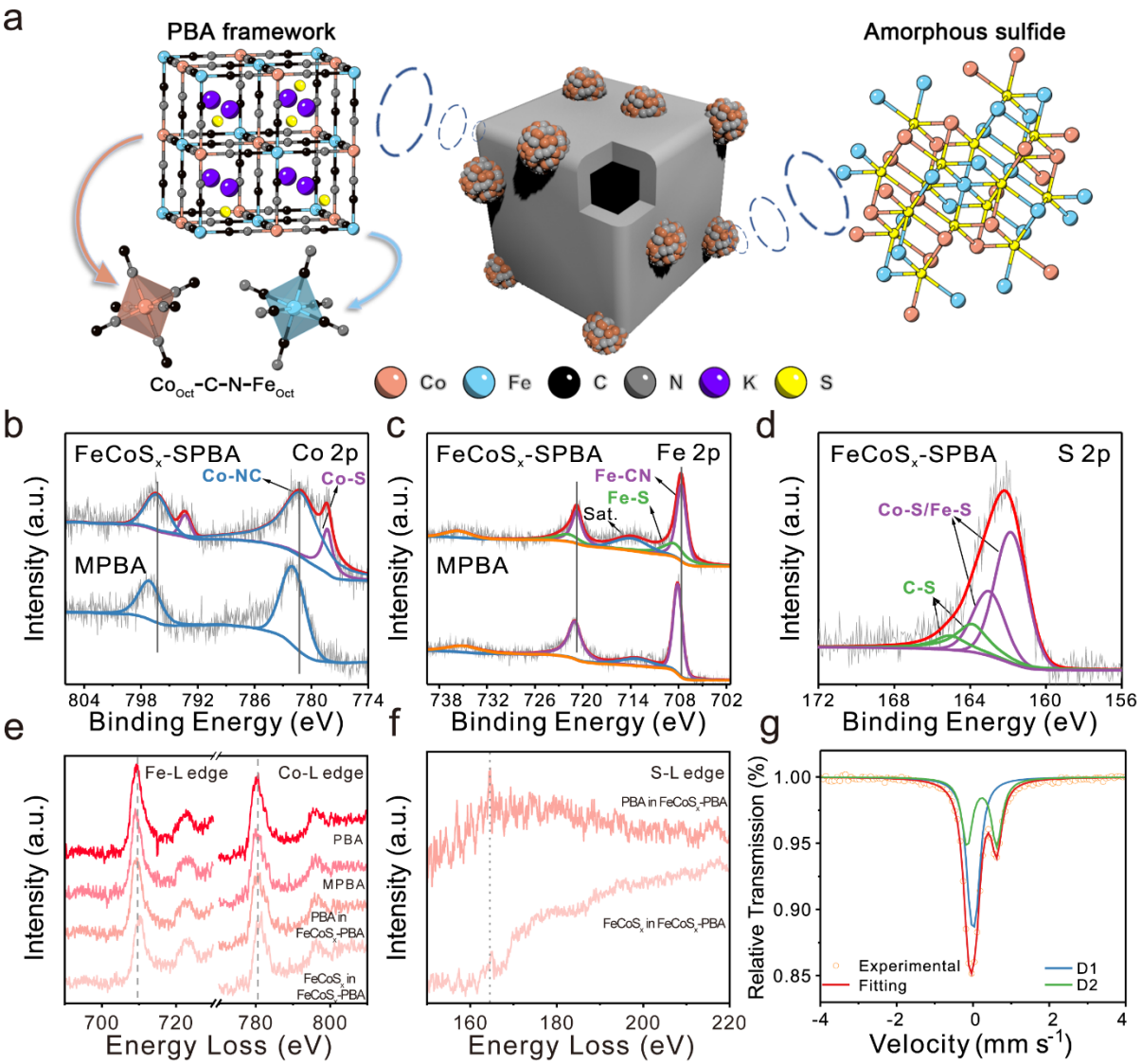

Figure 2. (a) Schematic diagram of $FeCoS_x$-PBA. (b) Co 2p and (c) Fe 2p XPS spectra of the of $FeCoS_x$-PBA and MPBA. (d) S 2p XPS spectra of $FeCoS_x$-PBA. (e) Co $L_{2,3}$ and Fe $L_{2,3}$ edge EELS spectra of PBA, MPBA, and $FeCoS_x$-PBA. (f) S $L_{2,3}$ edge EELS spectra of $FeCoS_x$-PBA. (g) Mössbauer spectrum pattern of $FeCoS_x$-PBA.

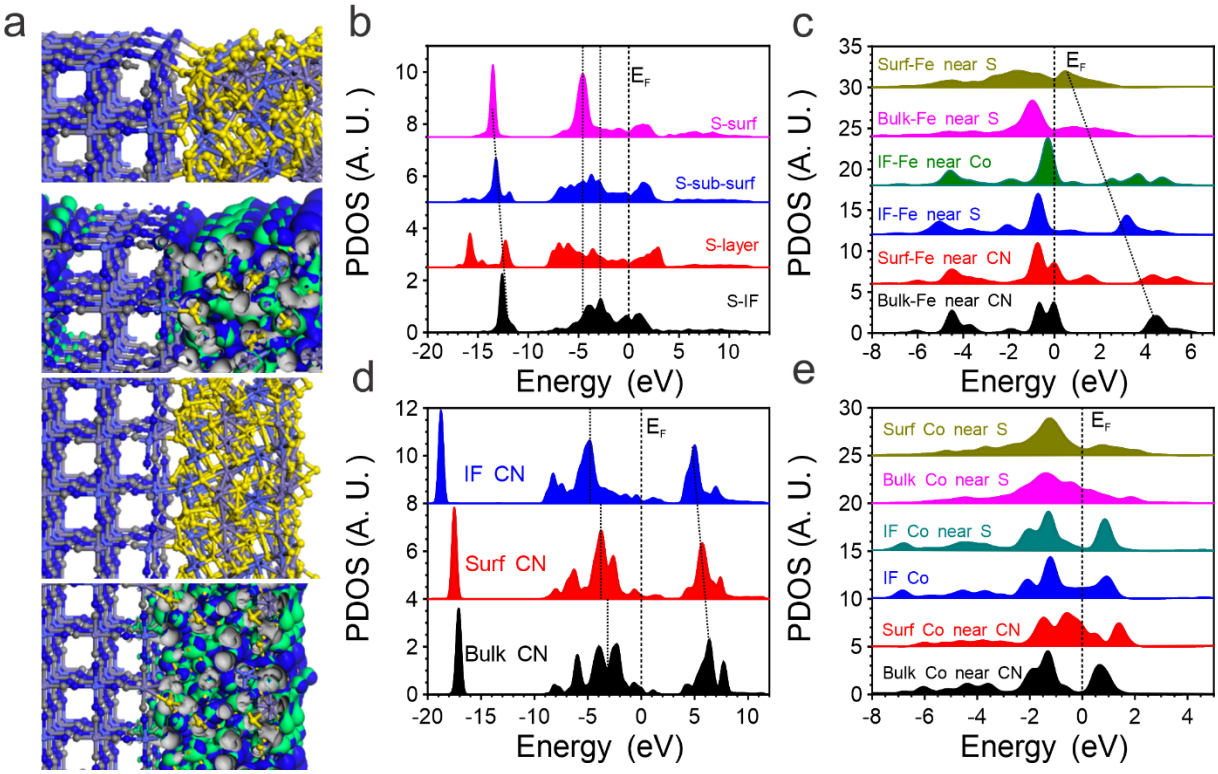

Figure 3. The electronic structures of $FeCoS_x$-PBA. (a) Structural configurations and real spatial 3D orbital contour plots of two different $FeCoS_x$-PBA system. (b) Site-dependent PDOSs of S in $FeCoS_x$-PBA. (c) Site-dependent PDOSs of Fe in $FeCoS_x$-PBA. (d) Site-dependent PDOSs of Co in $FeCoS_x$-PBA. (e) Site-dependent PDOSs of -CN in $FeCoS_x$-PBA.

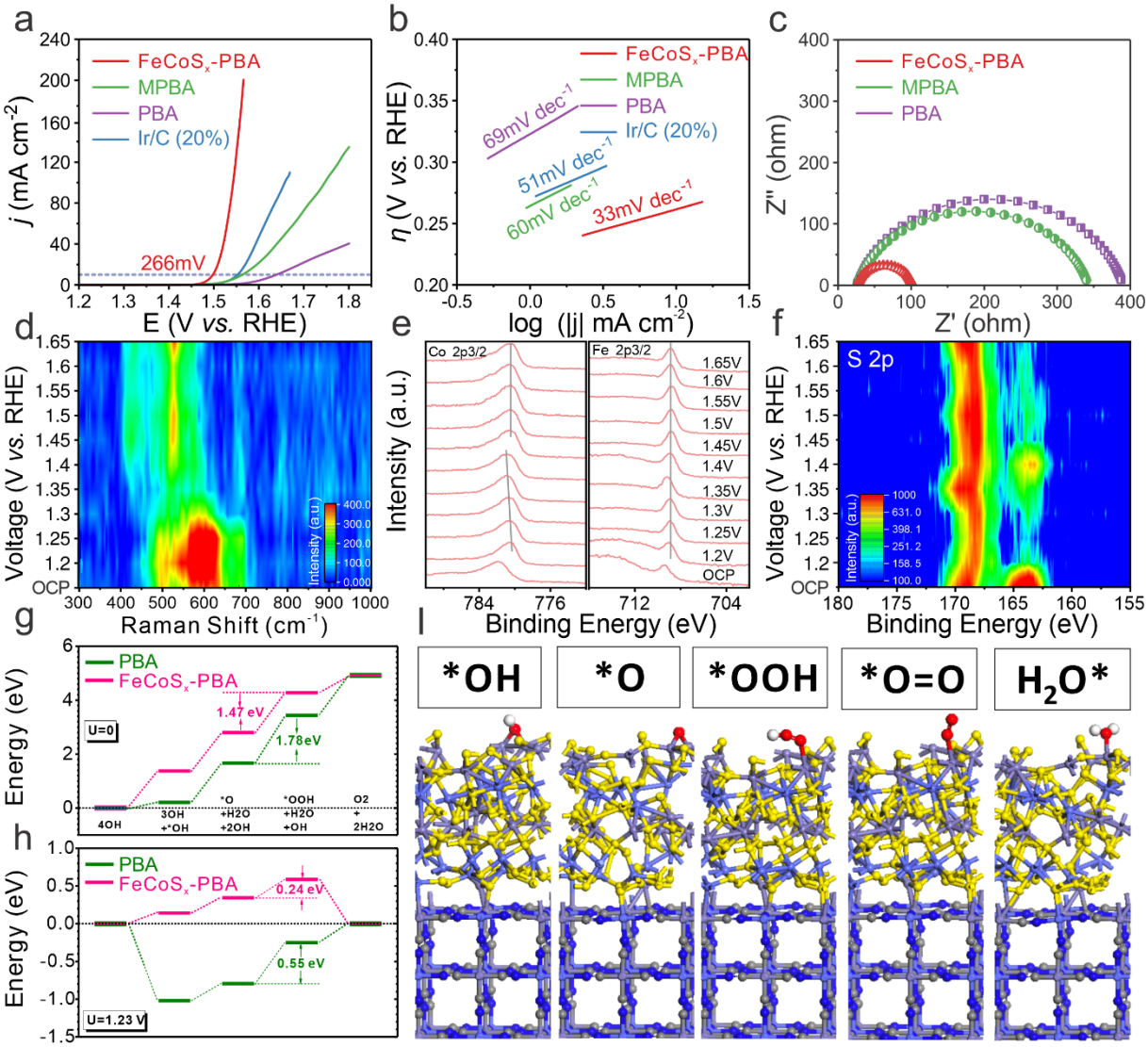

Figure 4. (a) Polarization curves and (b) Tafel plots of PBA, MPBA, $FeCoS_x$-PBA and commercial Ir/C (20%) in an O2-saturated 1 M KOH solution (scan rate 2 mV s^{-1}). (c) EIS spectra of PBA, MPBA and $FeCoS_x$-PBA. (d) *in-situ* Raman spectra of $FeCoS_x$-PBA during OER. (e) *quasi-in-situ* Co 2p3/2 and Fe 2p3/2 XPS spectra of $FeCoS_x$-PBA during OER. (f) *quasi-in-situ* S 2p XPS spectra of $FeCoS_x$-PBA during OER. (g) The OER reaction pathways of $FeCoS_x$-PBA and PBA in the alkaline environment at the equilibrium state (U = 0 V). (h) The OER reaction pathways of $FeCoS_x$-PBA and PBA in the alkaline environment with an applied potential of 1.23 V. (i) The structural configuration of key intermediates adsorptions on $FeCoS_x$-PBA.

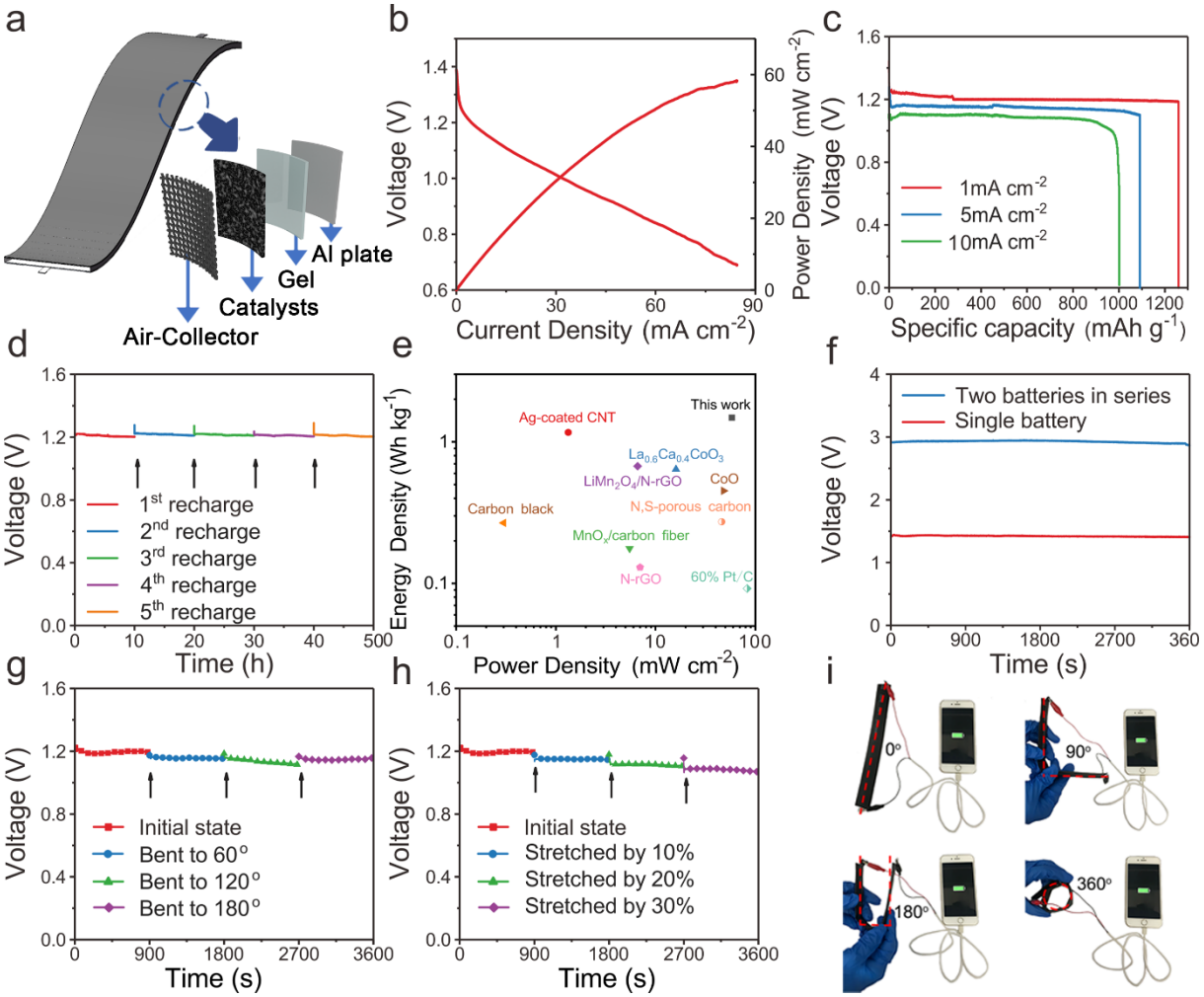

Figure 5. (a) Schematic diagram of flexible Al-air batteries. (b) Polarization and power density curves of the Al-air batteries. (c) Galvanostatic discharge curves at 1 mA cm^{-2}, 5 mA cm^{-2}, 10 mA cm^{-2} of Al-air batteries, respectively. (d) Discharge curves at 1 mA cm^{-2} and recharged by replacing Al foil. (e) Ragone plots of the Al-air batteries. The values reported for other energy storage devices are added for comparison. (f) open circuit voltage-time curves of one and two solid Al-air batteries. (g-h) Discharge curves of wearable Al-air batteries at different bending angles or stretching ratios at a discharge current of 1 mA. (i) Photographs of four batteries in series charging an iPhone with bending angle 0º, 90º, 180º, and 360º.

The electronic structure modified of amorphous Fe-Co-S sites embedded in Prussian blue analogues (PBA) hetero-nanoframes as high-performance oxygen evolution reaction (OER) and flexible Al-air battery electrocatalysts. The morphology and structure advantages enable excellent activity and superior stability toward the OER. Density functional theory calculations reveal the introduction of $FeCoS_x$ layer to PBA will enhance the electron transfer and alleviates the overbinding effect of OH*.

Min Lu, Li An, Jie Yin, Jing Jin, Rui Yang, Bolong Huang,* Yang Hu, Yong-Qin Zhao, Pinxian Xi,* and Chun-Hua Yan

Electronic Engineering of Amorphous Fe-Co-S Sites in Hetero-nanoframes for Oxygen Evolution and Flexible Al-air Batteries